INTERNATIONAL JOURNAL FOR NUMERICAL METHODS IN FLUIDS
Int. J. Numer. Meth. Fluids **30**: 577–606 (1999)

RESOLUTION TO A THREE-DIMENSIONAL PHYSICAL OCEANOGRAPHIC PROBLEM USING THE NON-LINEAR GALERKIN METHOD

BERNARD DI MARTINO AND PIERRE ORENGA*

URA CNRS 2053, Systèmes Dynamiques, Énergétiques et Mécaniques Université de Corse, Quartier Grossetti, 20250 Corte, France

SUMMARY

This paper presents the numerical results concerning the adaptation of the non-linear Galerkin method to three-dimensional geophysical fluid equations. This method was developed by Marion and Temam to solve the Navier–Stokes two-dimensional equations. It allows a substantial decrease in calculation costs due to the application of an appropriate treatment to each mode based on its position in the spectrum. The large scales involved in the study of geophysical flow require that the earth's rotational effects and the existence of a high degree of stratification be taken into account. These phenomena play an important role in the distribution of the energy spectrum. It is shown here that the non-linear Galerkin method is very well-suited to the treatment of these phenomena. First, the method for the particular situation of a *rigid-lid with a flat bottom* is validated, for which the functional basis used is particularly well-adapted. Then the more general case of a domain exhibiting variable bathymetry is presented, which necessitates the use of the transformation σ, thus providing a study domain with a cylindrical configuration.

KEY WORDS: geophysical fluids; non-linear Galerkin method

1. INTRODUCTION

The aim of the present study is to solve the equations that rule the three-dimensional flow of geophysical fluids. This resolution is based on the characteristics of a special basis initially developed to solve shallow water equations and which satisfies the impermeability type boundary conditions [1,2]. The authors use an extension of this basis to the three-dimensional cylindrical domains to solve the geophysical equations by the classical Galerkin method. Although the basis is well-adapted to solving the equation system, the presence of non-linearity within the system leads to very high simulation costs.

Marion and Temam developed a variation of this Galerkin method that takes into consideration the spectral characteristics of flow: *the non-linear Galerkin method* (NLG). A certain number of adaptations of this NLG method have been carried out, mainly in the solution of the two-dimensional Navier–Stokes equations [3–5].

In a previous study, the authors adapted this method to solve shallow water equations expressed in terms of height and velocity [6]. The results revealed that, although this method

* Correspondence to: URA CNRS 2053, Systèmes Dynamiques, Énergétiques et Mécaniques Université de Corse, Quartier Grossetti, 20250 Corte, France.

CCC 0271–2091/99/130577–30$17.50

Received December 1997
Revised July 1998

allows substantial gains when processing non-linear terms, it can also be influenced by the large spectral distribution generated by the Coriolis force. In the present study, an adaptation of this method to the three-dimensional flow is proposed.

First, the model under study and the characteristics of the special basis used are presented. Then the case of a domain possessing a flat bottom and for which we suppose to verify the *rigid-lid* hypothesis is described. This particular case allows the authors to avoid those obstacles involved in the determination of water depth in addition to the transformation of the horizontal diffusion operator, which is awkward to implement. A series of numerical experiments allows a comparison to be made between the NLG method results and those generated in the classical manner.

In the second part of this study, the general case that corresponds to a domain with variable bathymetry is presented, for which the use of a σ-type geometrical transformation is necessary in order to use the special basis. This transformation allows the study domain to be modified so as to give it a cylindrical configuration, and also allows other difficulties, such as those linked to the presence of a free-surface boundary, to be avoided.

1.1. Position of the problem

1.1.1. Notations. Ω_x is the fluid surface at rest, Ω_x is a bounded open of $\mathbb{R}^2$ of boundary γ. The depth of the domain, denoted $H(x, y)$ is a strictly positive regular function defined on Ω_x. The fluid surface is a free-boundary denoted $\zeta(x, y, t)$. The fluid thus occupies a variable domain $\Omega(t)$ defined by

$$\Omega(t) = \{(x, y, z);\ (x, y) \in \Omega_x,\ z \in]-H(x, y),\ \zeta(x, y, t)[\}. \tag{1.1}$$

The boundary of this domain is denoted $\Gamma(t)$, $\Gamma(t) = \Gamma_s(t) \cup \Gamma_f \cup \Gamma_l(t)$, where $\Gamma_s(t)$, the free-surface of the domain, is defined by $\Gamma_s(t) = \Omega_x \times \zeta(x, y, t)$, Γ_f, the bottom of the domain, is defined by $\Gamma_f = \Omega_x \times H(x, y)$ and a lateral boundary, $\Gamma_l(t)$, is defined by $\Gamma_l(t) = \Gamma_l = \{(x, y, z);\ (x, y) \in \Omega_x,\ z \in]-H(x, y),\ \zeta(x, y, t)[\}$ (see Figures 1 and 2).

Vertical velocity plays a particular role in geophysical fluids. Thus, $\mathbf{V}(u_x, u_y, v_3)$ is noted as being the velocity of the fluid and $\mathbf{u}(u_x, u_y)$ as being its horizontal component.

The buoyancy term is represented by the variable $b(x, y, z, t)$, which expresses the density variations ρ of the fluid with respect to its reference value ρ_0. These variations depend on salinity and temperature.

μ and ν represent the coefficients of the turbulent dispersal in the horizontal plane and in the vertical direction respectively.

The authors write $(\cdot, \cdot)$ and $\|\cdot\|$, the scalar product and the norm in $L^2(\Omega)$ and $L^2(\Omega)^2$ and

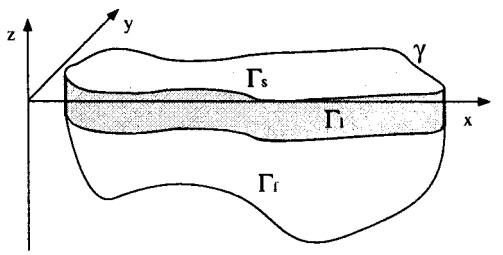

Figure 1. Study domain at rest ($\zeta = 0$), cross-section.

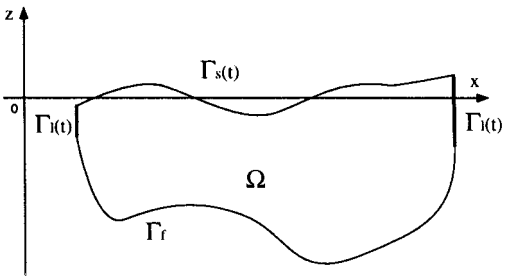

Figure 2. Vertical section of the domain.

$$\operatorname{curl}\mathbf{u}=\frac{\partial u_y}{\partial x}-\frac{\partial u_x}{\partial y};\qquad \operatorname{div}\mathbf{u}=\frac{\partial u_x}{\partial x}+\frac{\partial u_y}{\partial y};\qquad \alpha(\mathbf{u})=(-u_y,u_x);$$

$$\nabla p=\left(\frac{\partial p}{\partial x},\frac{\partial p}{\partial y}\right);\qquad \operatorname{Curl} q=\left(\frac{\partial q}{\partial y},-\frac{\partial q}{\partial x}\right);\qquad \Delta p=\frac{\partial^2 p}{\partial x^2}+\frac{\partial^2 p}{\partial y^2};$$

where p and q are scalar functions of Ω into $\mathbb{R}$.

1.1.2. Geophysical fluid equations. The authors use the equations that describe the three-dimensional flow of geophysical fluids presented in [7,8]. These equations are obtained by conserving the different state variables, including momentum, temperature, salinity and mass. They take into consideration the Boussinesq hypothesis that allows the variations in fluid density to be neglected, with the exception of those encountered in the pressure gradient. The quasi-hydrostatic hypothesis is then applied. This hypothesis allows the replacement of the vertical velocity equation by a hydrostatic equilibrium equation.

These equations are expressed in the following manner

$$\frac{\partial\mathbf{u}}{\partial t}+\mathbf{u}\nabla\mathbf{u}+v_3\frac{\partial\mathbf{u}}{\partial z}+\omega\alpha(\mathbf{u})-\frac{\partial}{\partial z}\left(\nu\frac{\partial\mathbf{u}}{\partial z}\right)-\mu\Delta\mathbf{u}=-\nabla q, \tag{1.2}$$

$$\frac{\partial b}{\partial t}+\mathbf{u}\cdot\nabla b+v_3\frac{\partial b}{\partial z}-\frac{\partial}{\partial z}\left(\nu_b\frac{\partial b}{\partial z}\right)-\mu_b\Delta b=0, \tag{1.3}$$

$$\operatorname{div}\mathbf{u}+\frac{\partial v_3}{\partial z}=0, \tag{1.4}$$

$$\frac{\partial q}{\partial z}=b, \tag{1.5}$$

$$\mathbf{V}=\mathbf{u}+v_3\mathbf{e}_z;\qquad q=\frac{p}{\rho_0}+gz\quad\text{and}\quad b=-\frac{\rho-\rho_0}{\rho_0}g, \tag{1.6}$$

where g is the acceleration of gravity, ω is twice the vertical component of the earth rotation vector, p is the pressure at the upper surface of the ocean and q the generalized pressure. A Cauchy–Kovalevsky-type system [9] is obtained by integrating at water level the diagnostic equations (1.4) and (1.5).

1.1.3. Boundary conditions. In order to simplify the present study, the authors will limit it to the particular case of a closed domain (with all boundaries being impermeable). The classical Dirichlet conditions ($\mathbf{u}=0$) associated with the Navier–Stokes equations are not applied to these solid boundaries but rather impermeability type conditions ($\mathbf{u}\cdot\mathbf{n}=0$) that are more suitable to geophysical fluid equations [10]. This condition is not sufficient and thus, a condition concerning the tangential component at the boundary is included [11].

If $\mathbf{n}_h$ is defined as the horizontal component of the exterior normal, then the boundaries are written as [12]

$$\begin{cases} \mathbf{u}\cdot\mathbf{n}_h = 0 & \text{on } \Gamma_l(t) \\ \text{Curl } \mathbf{u} \wedge \mathbf{n}_h = C_D\mathbf{u} & \text{on } \Gamma_l(t) \\ \text{grad } b\cdot\mathbf{n}_h = 0 & \text{on } \Gamma_l(t) \end{cases},$$

$$\begin{cases} u_3 = \dfrac{\partial\zeta}{\partial t} + \mathbf{u}\cdot\nabla\zeta & \text{on } \Gamma_s(t) \\ \nu\dfrac{\partial\mathbf{u}}{\partial z} - \mu \text{ div } \mathbf{u}\nabla\zeta + \mu \text{ curl } \mathbf{u} \text{ Curl } \zeta = \tau^s & \text{on } \Gamma_s(t) \\ \nu_b\dfrac{\partial b}{\partial z} - \mu_b\nabla b\cdot\nabla\zeta = F_b & \text{on } \Gamma_s(t) \end{cases},$$

$$\begin{cases} u_3 = -\mathbf{u}\cdot\nabla H & \text{on } \Gamma_f \\ \nu\dfrac{\partial\mathbf{u}}{\partial z} - \mu \text{ div } \mathbf{u}\nabla H + \mu \text{ curl } \mathbf{u} \text{ Curl } H = \tau^b & \text{on } \Gamma_f \\ \nu_b\dfrac{\partial b}{\partial z} - \mu_b\nabla b\cdot\nabla H = 0 & \text{on } \Gamma_f \end{cases},$$

where τ^s represents the effect of wind, τ^b describes the bottom friction, C_D, the 'drag coefficient', is assumed to be constant and F_b describes the scalar fluxes at the surface.

At the surface, the condition on the tangential component is particularly important as it describes the effects of wind stress. At the other boundaries, the conditions exert less of an influence on the global solution and are chosen homogenous for reasons of simplicity.

1.2. Basis

The authors took into consideration two possibilities in order to circumvent the difficulty linked to the presence of a free-surface. The first of these possibilities involves the addition of another hypothesis imposing a fixed surface, which is a reasonable hypothesis in certain cases. The flow must then satisfy an additional non-local constraint [9], the numerical implementation of which is only easily achievable on flat bottoms.

The second approach consists of applying the transformation σ that allows work on a cylindrical domain. The latter approach is more general, although the numerical solving is more problematic.

For both of these approaches, the resolution domain is a cylinder whose height is one unit ($\Omega = \Omega_x \times]0, 1[$).

1.2.1. Special basis for velocity. The following functional space to the fluid velocity is defined

$$\mathscr{V} = \left\{ \boldsymbol{\varphi} \in L^2(\Omega)^2 / \text{div } \boldsymbol{\varphi} \in L^2(\Omega), \text{ curl } \boldsymbol{\varphi} \in L^2(\Omega), \frac{\partial\boldsymbol{\varphi}}{\partial x_3} \in L^2(\Omega)^2; \boldsymbol{\varphi}\cdot n = 0 \text{ on } \Gamma \right\}. \tag{1.7}$$

$\mathscr{V}$, equipped with its natural norm, is algebraically and topologically included in $H^1(\Omega)^2$ if the domain is smooth enough [1].

A basis of this functional space can be obtained by extending the results generated by the study of shallow water equations that are briefly recalled below.

It is supposed that Ω_x simply connects to simplify. Let $\{p_i\}$ and $\{q_i\}$ be the two orthogonal basis obtained by solving respectively, the two following scalar problems [1]

$$Pg: \begin{cases} -\Delta p = \lambda p & \text{in } \Omega_x \\ \text{grad } p \cdot n = 0 & \text{on } \gamma \end{cases}, \qquad Pr: \begin{cases} -\Delta q = \mu q & \text{in } \Omega_x \\ q = 0 & \text{on } \gamma \end{cases}.$$

An orthogonal basis of $L^2(\Omega)$ and $\mathscr{V}$ is obtained, given by

$$\{\text{grad } p_i \cos(j\pi x_3);\ i \in \mathbb{N}^*, j \in \mathbb{N}\} \cup \{\text{Curl } q_i \cos(j\pi x_3);\ i \in \mathbb{N}^*, j \in \mathbb{N}\},$$

where $\text{grad } p_i \cos(j\pi x_3)$ and $\text{Curl } q_i \cos(j\pi x_3)$ verify

$$P: \begin{cases} -\Delta \mathbf{u} = \lambda \mathbf{u} & \text{in } \Omega_x \\ \mathbf{u} \cdot \mathbf{n} = 0 & \text{on } \Gamma_1 \\ \text{curl } \mathbf{u}\alpha(\mathbf{n}) = 0 & \text{on } \Gamma_1 \end{cases}.$$

It should be noted that when the domain Ω_x is not simply connected, then the set of the divergent and curl nil functions are not reduced to zero. Then, to the above set, an orthogonal basis of the functional space associated with the eigenvalue zero must be added [1]. The dimension of this space is equal to the number of islands and its study does not present any inherent difficulties.

1.2.2. A few characteristics. The authors dispose of the following characteristics, which are particularly useful to the numerical solution

$$\{\text{grad } p_i \cos(j\pi x_3);\ i \in \mathbb{N}^*, j \in \mathbb{N}\} \text{ is a basis of } \{\boldsymbol{\varphi} \in \mathscr{V};\ \text{curl } \boldsymbol{\varphi} = 0\},$$

$$\{\text{Curl } q_i \cos(j\pi x_3);\ i \in \mathbb{N}^*, j \in \mathbb{N}\} \text{ is a basis of } \{\boldsymbol{\varphi} \in \mathscr{V};\ \text{div } \boldsymbol{\varphi} = 0\}.$$

The barotropic component of flow corresponds to the mean velocity of the water column. The characteristics of the basis allow an easy access to this component. One only needs to eliminate the fluctuations about this mean by eliminating the modes for which $j \neq 0$. The baroclinic component represents the fluctuations about this mean value.

Finally, for the *rigid-lid* hypothesis, the authors have indicated the presence of a non-local constraint. This constraint is described by the relationship

$$\text{div}\left(H \int_{-H}^{0} \mathbf{u}(x, y, z)\, dz \right) = 0. \tag{1.8}$$

For the case of a flat bottom, it is easy to take from the above described basis, a basis that satisfies this constraint. There is need only to eliminate the barotropic component whose divergence is not zero.

1.2.3. Elevation basis. The function representing the elevation is a scalar function defined on Ω_x. It will be approach by using an orthogonal basis of $H^1(\Omega_x)$ that is built on the set of functions $\{p_i\}$, solutions of (Pg). The choice of this basis seems to be the most natural one, but it brings some very strong properties to the barotrope velocity elevation coupling [6], which will be described in the last section of this paper.

1.2.4. Basis for the other scalar variables. The scalar terms are approached by using a basis of $H^1(\Omega)$. This basis can be obtained from the spectral problem (Pg). By using the properties of the space tensorial product, one can deduce that the set

$$\{p_i \cos(j\pi x_3);\ i\in\mathbb{N}^*, j\in\mathbb{N}\} \tag{1.9}$$

forms an orthogonal basis of $H^1(\Omega)$ and $L^2(\Omega)$. The choice of this basis will give rise to strong properties to the velocity–pressure coupling.

2. APPROACH FOR A PARTICULAR CASE: HYPOTHESIS OF A RIGID-LID AND A FLAT BOTTOM

It is assumed that the study domain presents a *flat bottom*. If this is the case then the properties of the special basis allows the use of the rigid-lid hypothesis, which simplifies solving the problem. In particular, the authors do away with the solving of a non-linear hyperbolic equation describing the surface evolution. Thus, $\zeta(x, y, t) = 0$ is obtained for all values of t.

2.1. Solving using the Galerkin method

2.1.1. Weak formulation. Set $(\mathbf{u}_0, b_0)\in L^2(\Omega)^2 \times L^2(\Omega)$; thus, $(\mathbf{u}, b)$, the solution of

$$\begin{aligned}
&\left(\frac{\partial \mathbf{u}}{\partial t}, \boldsymbol{\varphi}\right) - \frac{1}{2}(\mathbf{u}^2, \operatorname{div}\boldsymbol{\varphi}) + (\operatorname{curl}\mathbf{u}\alpha(\mathbf{u}), \boldsymbol{\varphi}) + \left(v_3\frac{\partial \mathbf{u}}{\partial z}, \boldsymbol{\varphi}\right) + (\omega\alpha(\mathbf{u}), \boldsymbol{\varphi})\\
&= -\left(\int_{-z}^{0} b(\xi)\,\mathrm{d}\xi, \operatorname{div}\boldsymbol{\varphi}\right) + \int_{\Omega_x} [\tau^{\mathrm{s}}\boldsymbol{\varphi}(x, y, 1) - \tau^{\mathrm{b}}\boldsymbol{\varphi}(x, y, 0)]\,\mathrm{d}\Omega_x\\
&-\left(\nu\frac{\partial \mathbf{u}}{\partial z}, \frac{\partial \boldsymbol{\varphi}}{\partial z}\right) - \mu(\nabla\cdot\mathbf{u}, \nabla\cdot\boldsymbol{\varphi}) - \mu(\operatorname{curl}\mathbf{u}, \operatorname{curl}\boldsymbol{\varphi}) \quad \forall\boldsymbol{\varphi}\in\mathscr{V},
\end{aligned} \tag{2.1}$$

$$\begin{aligned}
&\left(\frac{\partial b}{\partial t}, \phi\right) + (\mathbf{u}\nabla b, \phi) + \left(v_3\frac{\partial b}{\partial x_3}, \phi\right) = \int_{\Omega_x} F^{\mathrm{b}}\phi(x, y, 0)\,\mathrm{d}\Omega_x - \left(v_b\frac{\partial b}{\partial x_3}, \frac{\partial \phi}{\partial x_3}\right) - \mu_b(\nabla b, \nabla\phi)\\
&\quad \forall\phi\in H^1(\Omega),
\end{aligned} \tag{2.2}$$

is sought. The existence of a solution to this weak problem has been demonstrated by Lions *et al.* [9].

2.1.2. Seeking an approximate solution. The authors search $\{\mathbf{u}_n(\mathbf{x}, t), b_m(\mathbf{x}, t)\}$ for an approximate solution to the above equation system. To do this, they use the following decompositions

$$\mathbf{u}_n(\mathbf{x}, t) = \sum_{i=1}^{n} \mathscr{X}_i(t)\boldsymbol{\varphi}_i(\mathbf{x}), \tag{2.3}$$

$$b_m(\mathbf{x}, t) = \sum_{i=1}^{m} \mathscr{Y}_i(t)\phi_i(\mathbf{x}), \tag{2.4}$$

and hence

$$v_{3_n}(\mathbf{x}, t) = \sum_{i\ \text{baroclinic} < n} \mathscr{X}_i(t)\int_z^1 \operatorname{div}(\boldsymbol{\varphi}_i(x, y, s))\,\mathrm{d}s, \tag{2.5}$$

$$q_m(\mathbf{x}, t) = -\sum_{i=1}^{m} \mathscr{Y}_i(t)\int_z^1 \phi_i(x, y, s)\,\mathrm{d}s + \frac{P_a}{\rho_0}. \tag{2.6}$$

The solution to the equation systems (2.1) and (2.2) can be approached by solving the system made up of $(m+n)$ first-order differential equations having constant coefficients, which is written in the following way:

$$\dot{\mathscr{X}}_i = \sum_{j=1}^{n} \mathscr{X}_j XX(i,j) + \sum_{j=1}^{m} \mathscr{Y}_j XY(i,j) + \sum_{j=1}^{n} \sum_{k=1}^{n} \mathscr{X}_j \mathscr{X}_k XXX(i,j,k), \tag{2.7}$$

$$\dot{\mathscr{Y}}_i = \sum_{j=1}^{m} \mathscr{Y}_j YY(i,j) + \sum_{j=1}^{n} \sum_{k=1}^{m} \mathscr{X}_j \mathscr{Y}_k YXY(i,j,k), \tag{2.8}$$

$$\mathscr{X}_i(0) = \mathscr{X}_{i0}; \qquad \mathscr{Y}_i(0) = \mathscr{Y}_{i0}; \tag{2.9}$$

where the terms XX, XY, XXX, YY and YXY are constant and represent integrals on the study domain of basis function combinations.

2.2. Non-linear Galerkin method

2.2.1. Spectral behaviour. One of the difficulties in simulating turbulent flow is linked to the presence of a wide range of interacting scales. Simulation thus necessitates that a large number of degrees of freedom be taken into account. This leads to important calculation costs due to the presence of non-linear terms.

Inspired by the results obtained to solve of the Navier–Stokes equations by using the non-linear Galerkin method, the authors will deduce simplified behavioural laws for the smallest structures set in motion. In the Navier–Stokes equations, only the non-linear terms are responsible for these extensive scale variabilities. Conversely, the equations presented here exhibit transfer sources that are more varied. Nevertheless, there exists an energy cascade that is similar to that observed in the Navier–Stokes equations, and from which one can provide the main principle by using the description given by Charney [13] (see Figure 3).

Every mode undergoes constraints due to the wind. Even if it is assumed that this wind is fairly constant, there is still an infinite number of modes stimulated by the boundary conditions. These modes will exhibit a different behaviour with respect to this stimulation based on their position in the spectrum. They can be grouped into three categories:

At the largest scales, the flow is essentially two-dimensional (barotropic component). These barotropic modes are not very sensitive to viscous dispersal due to their position in the low frequencies. They transmit their energy mainly in the two following ways:

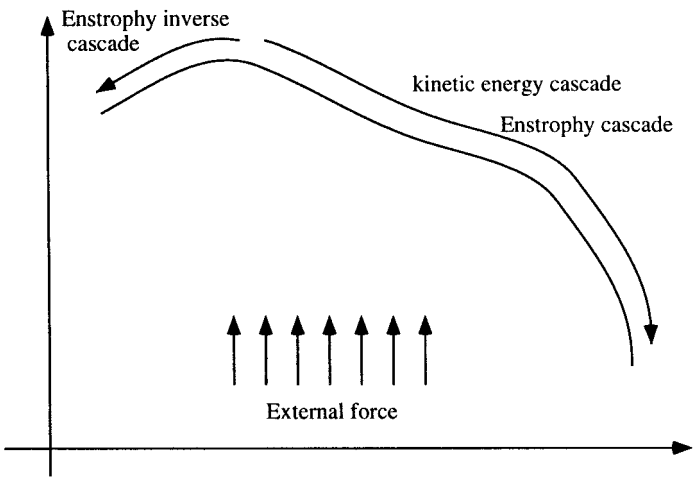

Figure 3. Energy spectrum according to Charney.

– at modes of greater dimension, through an inverse kinetic energy cascade. The surplus energy is then dispersed by the boundaries conditions.
– at modes of smaller dimension, through an enstrophic barotropic cascade. This energy is then dispersed by viscous constraints.

At the medium scales, it is the barocline modes that are excited. These modes will principally redistribute their energy as a baroclinic energy cascade, thus transporting the energy to the viscous dispersal area. This cascade is similar to the energy cascade predicted by Kolmogorov for Navier–Stokes equations. These modes also contribute to the apparition of potential energy via a destabilization of the pressure field stratification.

Finally, at the very small scales, the energy provided by the surface forces is insufficient to oppose the viscous dispersal constraints.

In the geophysical flows, the distribution of energy through the baroclinic, barotropic entrophy and inverse barotropic energy cascades originate mainly from the force of Coriolis and the pressure gradient. The non-linear advection terms have a minor role if the dimensions of the domain are large enough. Indeed, the ratio between the non-linear terms and the force of Coriolis is the Rossby number, defined as

$$Ro = \frac{\text{Non-linear terms}}{\text{Force of Coriolis}} = \frac{U}{\omega L}.$$

For typical values $U \sim 1\ \mathrm{m\,s^{-1}}$, $\omega \sim 10^{-4}\ \mathrm{s^{-1}}$ and $L \sim 10^{6}$ m, the Rossby number is in the order of 10^{-2} [14]. Thus, the advection terms occurring in the calculation of velocity can often be omitted.

The phenomena just described allows the schematization of the total energy exchanges within the flow. To these exchanges must be added the balance that occurs with the pressure terms. The spectral presentation of the scalar terms reveals the presence of a cascade similar to that observed for velocity [15]. It is mainly the presence of these cascades generated by the dispersal effects that justifies the utilization of the non-linear Galerkin method.

2.2.2. Method description. Marion and Temam used these dispersal properties of the equations to develop a new numerical method. Indeed, the Galerkin method is based on a spectral representation of flow and if the energy cascade is taken into account while solving the problem then an appropriate treatment can be applied to each mode based on its location in the spectrum. The more distant modes in the spectrum represent small size structures that have little energy and possess a small range of variability. These structures show very short response times and practically 'adhere' to the evolution of the larger structures [16]. It is costly and often very difficult to seek to accurately represent these structures. It is preferable to simply extract from them the most essential information that is capable of modifying the large scale flow behaviour. If care is taken to limit the losses of information on the small structures, e.g. if these losses are in the order of the precision of the numerical integration method, then the result of simulation is comparable in terms of quality with that generated using the classical Galerkin method. The savings in calculation costs can be very high when using a simplified and linearized expression of small structure evolution. This method generally generated a better numeric stability by eliminating the oscillation interferences associated with the small structures.

For the geophysical flow, the modelling of phenomena occurring at scales below the spatial or temporal discretization remains highly approximated. The NLG method is used to take into consideration the smaller structures, thus allowing a better approach of the solution and at a reasonable cost.

2.2.3. Selection of the cut-off frequencies. To use the NLG method, a cut off frequency must be identified, which is identified by the index n_1 (or m_1) of the associated eigenfunction and which allows the separation of the small and large components. This frequency depends on the flow kinetics and can vary substantially over time. Among the different two-dimensional resolution methods tested, that which compares the kinetic (or potential) energy ratios of the small and large components to a reference value was retained. A different cut-off frequency is associated with each unknown.

In the following, the small components are presented by topping them with the symbol $\hat{}$.

For n and n_1 (respectively m and m_1), which belong to $\mathbb{N}$, $n_1 < n$ (respectively $m_1 < m$), the following projection operators are defined

- $\mathbf{P}_{n_1}$ the projection $L^2(\Omega)^2$ on the space generated by the functions $\boldsymbol{\varphi}_1, \ldots, \boldsymbol{\varphi}_{n_1}$.
- $\mathbf{Q}_{n_1}$ the projection $L^2(\Omega)^2$ on the space generated by the functions $\boldsymbol{\varphi}_{n_1+1}, \ldots, \boldsymbol{\varphi}_n$.
- $\mathbf{P}_{\mathbf{b}m_1}$ the projection $L^2(\Omega)$ on the space generated by the functions $\phi_1, \ldots, \phi_{m_1}$.
- $\mathbf{Q}_{\mathbf{b}m_1}$ the projection $L^2(\Omega)$ on the space generated by the functions $\phi_{m_1+1}, \ldots, \phi_m$.

We write $\mathbf{u}_{n_1} = \mathbf{P}_{n_1}(\mathbf{u})$, $\hat{\mathbf{u}}_{n_1} = \mathbf{Q}_{n_1}(\mathbf{u})$, $b_{m_1} = \mathbf{P}_{\mathbf{b}m_1}(b)$, $\hat{b}_{m_1} = \mathbf{Q}_{\mathbf{b}m_1}(b)$ as well as $\mathbf{V}_{n_1} = \mathbf{u}_{n_1} + v_{3_{n1}}$ and $\hat{\mathbf{V}}_{n_1} = \hat{\mathbf{u}}_{n_1} + \hat{v}_{3_{n1}}$ where $\hat{v}_{3_{n1}} = v_{3_n} - v_{3_{n1}}$.

The cut-off frequencies are then obtained by taking the smallest values of n_1 and m_1 that satisfy the following ratios

$$\frac{Ec(\hat{\mathbf{V}}_{n_1})}{Ec(\mathbf{V}_{n_1})} < \varepsilon_{\mathbf{u}}, \qquad \frac{Eb(\hat{b}_{m_1})}{Eb(b_{m_1})} < \varepsilon_b, \tag{2.10}$$

where $\varepsilon_{\mathbf{u}}$ and ε_b are values that represent the accuracy of the numeric integration diagrams associated with $\mathbf{u}$ and b. Ec represents the kinetic energy associated with the flow and Eb is an equivalent expression for the scalar terms.

By using the orthonormal characteristics of the basis presented in Section 1.2.1, in addition to the fact that vertical velocity is also broken down on an orthonormal basis, one obtains

$$Ec(\mathbf{V}_n) = \frac{1}{2}\|\mathbf{u}_n\|^2_{L^2} + \frac{1}{2}\|v_{3_n}\|^2_{L^2} = \frac{1}{2}\sum_{i=1}^{n} \mathscr{X}_i^2 + \frac{1}{2}\sum_{i \text{ baroclinic} < n} \mathscr{X}_i^2 \left| \int_z^1 \operatorname{div}(\boldsymbol{\varphi}_i(x, y, s))\, \mathrm{d}s \right|^2, \tag{2.11}$$

$$Eb(b_m) = \frac{1}{2}\|b_m\|^2_{L^2} = \frac{1}{2}\sum_{i=1}^{m} \mathscr{Y}_i^2. \tag{2.12}$$

We write Δt as the temporal discretization step and define $\tau = nblok * \Delta t$ as the temporal period (corresponding to *nblok* time steps) during which the small components of the flow ($\hat{\mathbf{u}}_{n_1}$ and $\hat{b}_{m_1}$) are assumed to be constant (Figure 4).

It is assumed that at time t_j, the values of all of the coefficients $\mathscr{X}_i$ and $\mathscr{Y}_i$ are known. This instant is taken as a starting point of the NLG method. In the sections below, the method used to evaluate the different terms over the time interval $[t_j, t_j + \tau]$ discretized into *nblok* segments with a length of Δt, will be indicated.

2.2.4. Application to the non-linear terms of velocity advection. The advection terms present in the momentum equation are processed in the same way as in the Navier–Stokes equations [3]. The authors will briefly recall the general outline of this procedure.

It is noted that $B(\mathbf{u}_n, \mathbf{u}_n)$ is the non-linear term and the velocity decomposition indicated above is applied

$$B(\mathbf{u}_n, \mathbf{u}_n) = B(\mathbf{u}_{n_1}, \mathbf{u}_{n_1}) + B_{\text{int}}(\mathbf{u}_{n_1}, \hat{\mathbf{u}}_{n_1}); \tag{2.13}$$

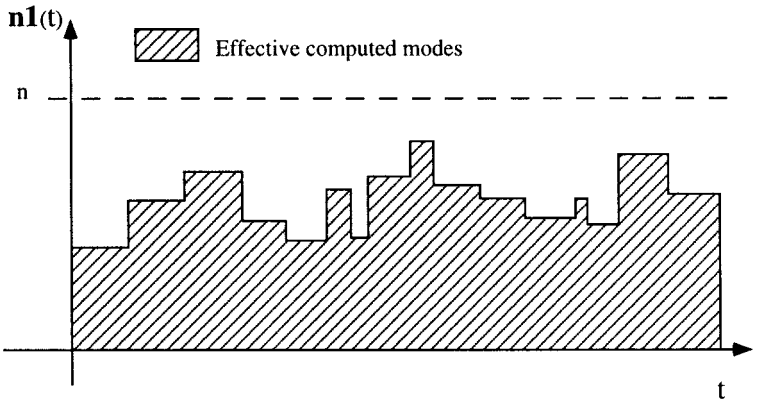

Figure 4. Evolution of the cut-off frequency n_1.

where

$$B_{\text{int}}(\mathbf{u}_{n_1}, \hat{\mathbf{u}}_{n_1}) = B(\mathbf{u}_{n_1}, \hat{\mathbf{u}}_{n_1}) + B(\hat{\mathbf{u}}_{n_1}, \mathbf{u}_{n_1}) + B(\hat{\mathbf{u}}_{n_1}, \hat{\mathbf{u}}_{n_1}) \tag{2.14}$$

represents the sum of the interactions in which the small structures appear.

The theoretical results obtained by Foias *et al.* [17] allow the demonstration that the evolution of $\hat{\mathbf{u}}_{n_1}$ is small if the value n_1 is chosen large enough. It is then possible to consider the influence of $B_{\text{int}}(\mathbf{u}_{n_1}, \hat{\mathbf{u}}_{n_1})$ as being constant for short time periods [5].

If the energy cascade is taken into account, then it is reasonable to assume that the component $B(\hat{\mathbf{u}}_{n_1}, \hat{\mathbf{u}}_{n_1})$ is an order of magnitude lower than the components $B(\hat{\mathbf{u}}_{n_1}, \mathbf{u}_{n_1})$. This hypothesis has been experimentally validated in two-dimensional equations for a value of n_1 that is large enough.

An estimation of the non-linear terms (TNL) during the assessment of the large structures is given by the equation

$$\text{TNL}(t + \Delta t) = \int_t^{t+\Delta t} \mathbf{P}_{n_1}(B(\mathbf{u}_{n_1}(\theta), \mathbf{u}_{n_1}(\theta))\, \mathrm{d}\theta + \Delta t B_{\text{int}}(\mathbf{u}_{n_1}(t_j), \hat{\mathbf{u}}_{n_1}(t_j))). \tag{2.15}$$

At time $t_j + \tau$, the estimation of the small components of flow is based on a simplified law that only uses the interactions amongst large structures

$$\widehat{\text{TNL}}(t_j + \tau) = \tau \mathbf{Q}_{n_1}(B(\mathbf{u}_{n_1}(t_j + \tau), \mathbf{u}_{n_1}(t_j + \tau))). \tag{2.16}$$

2.2.5. Application to the non-linear terms of pressure advection. The pressure advection term can be treated in the same way as the velocity advection term. Indeed, if $C(\mathbf{u}_n, b_m)$ is written as being this term and if it is applied to the decomposition of the two unknowns, the following expression is obtained

$$C(\mathbf{u}_n, b_m) = C(\mathbf{u}_{n_1}, b_{m_1}) + C_{\text{int}}(\mathbf{u}_{n_1}, b_{m_1}), \tag{2.17}$$

with

$$C_{\text{int}}(\mathbf{u}_{n_1}, b_{m_1}) = C(\hat{\mathbf{u}}_{n_1}, b_{m_1}) + C(\mathbf{u}_{n_1}, \hat{b}_{m_1}) + C(\hat{\mathbf{u}}_{n_1}, \hat{b}_{m_1}). \tag{2.18}$$

This term is very similar to that examined in the previous paragraph and an identical treatment is applied to it. The authors note, however, that the advection of scalar magnitudes plays a more important role than the one of velocity in geophysical fluids. It allows a distortion of the

fluid stratification, which even if this deformation remains weak, generates important horizontal pressure gradients.

Since $\hat{\mathbf{u}}_{n_1}$ and $\hat{b}_{m_1}$ are small as compared with $\mathbf{u}_{n_1}$ and b_{m_1}, it is reasonable to assume that the influence of component $C_{\text{int}}(\mathbf{u}_{n_1}, b_{m_1})$ is low in comparison with that of component $C(\mathbf{u}_{n_1}, b_{m_1})$ (for values of n_1 and m_1 that are large enough). The authors then apply to $C_{\text{int}}(\mathbf{u}_{n_1}, b_{m_1})$ the same hypothesis that was applied to $B_{\text{int}}(\mathbf{u}_{n_1}, \hat{\mathbf{u}}_{n_1})$.

In the same way, in the calculation of $C_{\text{int}}(\mathbf{u}_{n_1}, \hat{\mathbf{u}}_{n_1})$, the term $C(\hat{\mathbf{u}}_{n_1}, \hat{b}_{m_1})$ is an order of magnitude lower than the other two terms and can be omitted.

The expressions retained for the calculation of the scalar advection terms are thus as follows:

$$\text{TADV}(t+\Delta t) = \int_t^{t+\Delta t} \mathbf{P}_{\text{b}m_1}(C(\mathbf{u}_{n_1}(\theta), \mathbf{u}_{n_1}(\theta)))\,\mathrm{d}\theta + \Delta t C_{\text{int}}(\mathbf{u}_{n_1}(t_j), \hat{b}_{m_1}(t_j)), \tag{2.19}$$

$$\widehat{\text{TADV}}(t_j+\tau) = \tau \mathbf{Q}_{\text{b}m_1}(C(\mathbf{u}_{n_1}(t+\tau), b_{m_1}(t+\tau))). \tag{2.20}$$

TADV represents the advective component for the large scalar modes and $\widehat{\text{TADV}}$ is the advective component intervening in the evaluation of the small scalar structures.

These estimates are validated by the obtaining of simulation results comparable with those generated by the classical Galerkin method.

2.2.6. Application to the Coriolis term. If the total energy balance of flow is considered, then it can be established that the Coriolis force does not contribute to this balance. Nevertheless, its role in the transfer of energy in geophysical flow remains fundamental. The Rossby number, which is generally lower than 1%, indicates that the energy exchanges that originate from the Coriolis force are much more important than are those generated by the advective terms.

The Coriolis force is perpendicular to the flow and generates an energy cascade in the same way as the non-linear advection terms. This cascade is responsible for the development of complicated structures, the simplest expression of which is given by the Ekman spiral.

The special basis described in Section 1.2.1 is particularly well-adapted to represent velocity since it was constructed to satisfy the impermeable boundary conditions. But with the Coriolis force being orthogonal to the velocity, more modes are needed for a better representation of this term. For this reason, the GNL method is well-adapted to these equation even if the non-linear terms are neglected.

To obtain the simplified interaction laws existing between the large and small structures, three important observations must be made.

- Since the operator α brings about a rotation of $\pi/2$, one obtains $(\alpha(\boldsymbol{\varphi}_k), \boldsymbol{\varphi}_k) = 0$.
- The operator α only acts on the horizontal component of velocity and leaves its vertical component unchanged. Coupling between the modes can only occur between modes that possess the same vertical component. They are therefore two-dimensional.
- The typical scale associated with the Coriolis force is roughly the same as that associated with velocity as these two fields only differ by a rotation. The spectrum of the Coriolis force thus exhibits a cascade similar to the kinetic energy cascade.

By taking these characteristics into consideration in the numeric method, there is need only to retain the following expression for the assessment of small components

$$\widehat{\text{FC}}(t_j+\tau) = \tau \mathbf{Q}_{n_1}(\omega \wedge (\mathbf{u}_{n_1}(t+\tau))). \tag{2.21}$$

During the assessment of the largest components, it is necessary to keep the influence of $\hat{\mathbf{u}}_{n_1}$, as this term over long periods of time can modify the flow at the large scale. The role of this term is thus similar to that of the term $B_{\text{int}}(\mathbf{u}_{n_1}, \hat{\mathbf{u}}_{n_1})$ in the assessment of non-linear terms. As it only depends on $\hat{\mathbf{u}}_{n_1}$, this term is constant over the interval $[t_j, t_j+\tau]$ and one has

$$\mathrm{FC}(t+\Delta t)=\int_t^{t+\Delta t}\mathbf{P}_{n_1}(\omega\wedge(\mathbf{u}_{n_1}(\theta)))\,\mathrm{d}\theta+\Delta t\mathbf{P}_{n_1}(\omega\wedge(\hat{\mathbf{u}}_{n_1}(t_j))). \tag{2.22}$$

2.2.7. Application to the horizontal pressure gradient. The horizontal pressure gradient is the result of a modification in fluid stratification that is linked to both the flux conditions at the surface and to the advective transport of the scalar variables. A balance becomes established between the movement of kinetic energy and the potential energy associated with this modification in stratification. When the pressure decomposition is applied in the form of large and small components, the pressure gradient can be written in the following way

$$\nabla q_n=F(b_{m_1})+F(\hat{b}_{m_1}). \tag{2.23}$$

The choice of the scalar basis built by using the eigenfunctions associated with the problem (Pg) (Section 1.2.1) gives very strong characteristics between the equation vector and scalar. Indeed, one has the following scalar products

$$\left(\mathrm{grad}\,p_i\int_{x_3}^1\cos(j\pi\xi)\,\mathrm{d}\xi;\ \mathrm{grad}\,p_r\cos(s\pi x_3)\right), \tag{2.24}$$

as the $\{\mathrm{grad}\,p_i\}$ forms an orthogonal basis. These term are zero if i is not equal to r.

The authors apply the NLG method by evaluating the pressure forces using the following expressions

$$\mathrm{FGQ}(t+\Delta t)=\int_t^{t+\Delta t}\mathbf{P}_{n_1}(F(b_{n_1}(\theta)))\,\mathrm{d}\theta+\Delta t\mathbf{P}_{n_1}(F(\hat{b}_{n_1})(t_j)), \tag{2.25}$$

$$\widehat{\mathrm{FGQ}}(t_j+\tau)=\tau\mathbf{Q}_{n_1}(F(b_{n_1}(t_j+\tau))); \tag{2.26}$$

where FGQ represents the horizontal pressure gradient contribution on the larger structures and $\widehat{\mathrm{FGQ}}$ represents that of the smaller structures.

2.2.8. Application to the diffusion terms. When the diffusion coefficients are constant over the entire study domain, then the three-dimensional diffusion operator commutes with the projection operator L^2. Hence, this diffusion operator does not generate coupling between the different modes. Implementing a squaring method allows, in this case, the precise integration of the diffusion. Thus, for a coefficient $\mathscr{X}_i$, to which is associated a horizontal mode grad p_{i_x} (or Curl q_{i_x}), of eigenvalue λ_{i_x} and a vertical mode $\cos(i_z\pi z)$ associated with the eigenvalue $(i_z\pi)^2$, the integration between the times t_j and t_{j+1} is written

$$\mathscr{X}_{i,j+1}=\mathrm{e}^{-\kappa^2\Delta t}\mathscr{X}_{i,j}+\left[\frac{1-\mathrm{e}^{-\kappa^2\Delta t}}{\kappa^2}\right]f_i(\{\mathscr{X}_{l_x,j+1}\}_{1\le l_x\le n},\{\mathscr{Y}_{l_y,j+1}\}_{1\le l_y\le m}),$$
$$(\kappa^2=\mu\lambda_{i_x}+\nu(i_z\pi)^2), \tag{2.27}$$

where f_i represents the totality of the terms intervening in the equation with the exception of the diffusion terms and κ^2 is the eigenvalue associated with the three-dimensional mode.

Although the horizontal diffusion operator for geophysical fluids is generally considered to be constant, it is nonetheless common practice to use a finer modelling to represent the vertical effects. In the simplest cases, this modelling consists of defining a vertical profile of viscosity variations [18]. In more elaborate models, this modelling involves the calculation of this diffusion according to flow [19,20]. The application of this varying vertical viscosity is a source of energy exchanges, the nature of which is strongly linked to the viscosity profile. It is nevertheless possible to integrate the mean diffusion value by the formula given below. The fluctuating value is thus added to the function f_i.

This method is particularly efficient in the evaluation of small structures to which a high level of diffusion is associated. It allows the use of a larger integration step without generating too much numeric instability.

2.2.9. Classification of the eigenfunctions. The authors have not yet explained the manner in which the functions of the basis are classified. For the problem of shallow water, the natural classification is obtained by sorting the eigenvalues of problems (Pr) and (Pg) in increasing order. During the extension of the basis of the three-dimensional problem, however, they must add the effect of the vertical component. The most natural classification is, therefore, a classification based on increasing eigenvalues of the three-dimensional diffusion operator $\mu\Delta + \nu(\partial^2/\partial z^2)$.

This classification is easy for the case of a domain possessing a *flat bottom* with a constant vertical diffusion coefficient. If this fluid has a variable vertical diffusion profile then the value ν is replaced by its mean value on the domain. It is based on this classification that the large and small components are distinguished.

In much the same way, the three-dimensional modes of the scalar basis are classified in increasing order of the three-dimensional operators eigenvalues $\mu_b\Delta + \nu_b(\partial^2/\partial z^2)$.

2.3. Resolution algorithm

The resolution of the differential equations system is the only step that differs between usual and non-linear Galerkin method. The auhors describe this step.

1. The basis is constructed on the solutions to the spectral problems (Pr) and (Pg). These problems are solved by using a finite elements code (ModuleEF, Inria). The utilization of Hermit-type elements allows the direct access to the gradient and curl of the function without having to resort to a numeric derivation algorithm.
2. The initial conditions, as well as those boundaries conditions at the surface, can be obtained from experimental data but they are often provided in an empirical way.
3. The resolution of the equation system is based on an Euler scheme using a squaring method to integrate the diffusion terms. The scheme is implicit for the larger structures and explicitly for the smaller ones, these last structures only being expressed in relation to the larger structures. The authors have added a determination model for the values n_1 and m_1 that is called upon every *nblok* time steps. The values of *nblok*, $\varepsilon_{\mathbf{u}}$ and ε_b are initial parameters of the resolution.

The convergence criterion of the solution uses the comparison of the norm L^2 of the velocity and scalar fields between two successive iterations. The complete algorithm allows coupling between the velocity and the pressure equation, this last term presenting slower dynamics. This coupling is not presented in the following scheme. If it is noted that

$$f_i = \mathrm{TNL} + \mathrm{FC} + \mathrm{FGQ} + \mathbf{P}_{n_1}(\tau^{\mathrm{s}} - \tau^{\mathrm{b}}),$$
$$\hat{f}_i = \widehat{\mathrm{TNL}} + \widehat{\mathrm{FC}} + \widehat{\mathrm{FGQ}} + \mathbf{Q}_{n_1}(\tau^{\mathrm{s}} - \tau^{\mathrm{b}}),$$
$$g_i = \mathrm{ADV} + \mathbf{P}_{\mathbf{b}n_1}(F^{\mathrm{b}}),$$
$$\hat{g}_i = \widehat{\mathrm{ADV}} + \mathbf{Q}_{\mathbf{b}n_1}(F^{\mathrm{b}}),$$
$$\kappa^2 = \mu\lambda_{i_x} + \nu(i_z\pi)^2$$

and

$$\kappa_b^2 = \mu_b\lambda_{i_x} + \nu_b(i_z\pi)^2,$$

then the numerical scheme can be presented in the following manner

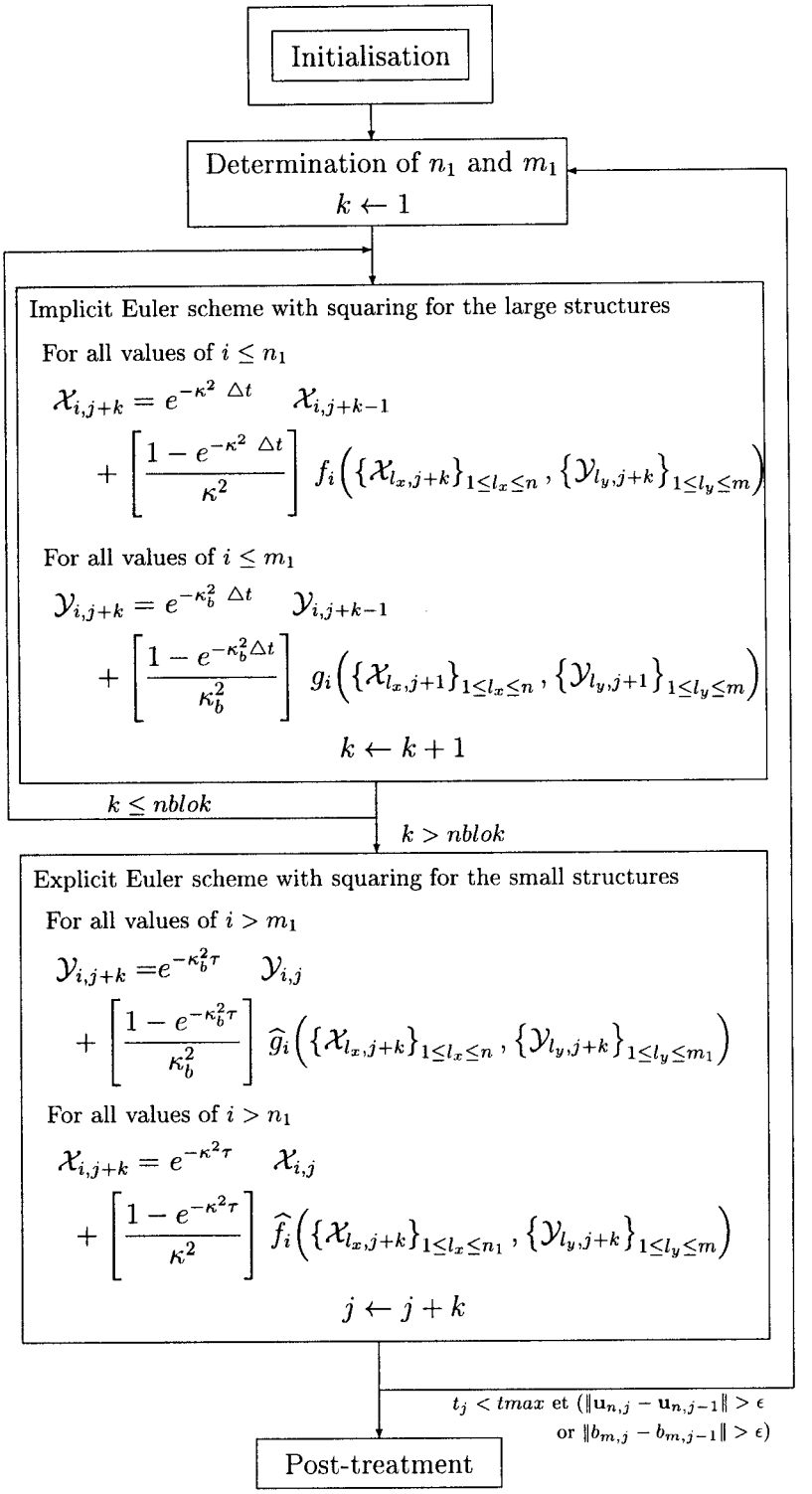

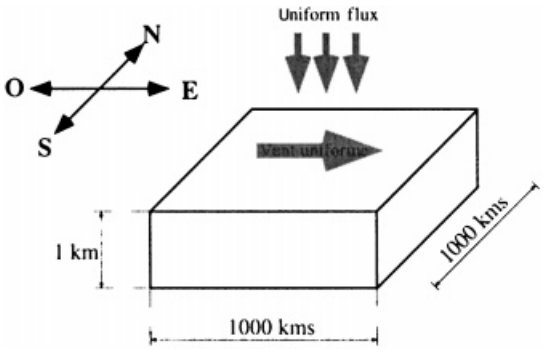

Figure 5. Simulation domain.

2.4. Numerical application

2.4.1. The studied domain and boundaries conditions. The choice of a square shaped study domain allows the eigenfunctions that are the solutions to the spectral problems (Pr) and (Pg) be directly obtained (which are hence sine and cosine function combinations). This in no way restricts the generality presented below and helps eliminate the numerical errors generated by the approximation of the eigenfunctions.

The length L_0 of this domain is 1000 km, which corresponds more or less to the dimensions of the western Mediterranean. The bathymetry $H(x, y)$, which is constant in this first approach, is in the order of 1000 m (see Figure 5).

For a domain of this size, the flow is mainly governed by the balance existing between the Coriolis force and the pressure forces. The advection terms for velocity can be omitted as the Rossby number is in the order of 10^{-3}. In order to reveal the energy distribution generated by the other flow components, the authors have not taken these velocity advection terms into consideration. Conversely, they play an important role in the pressure evolution equation.

The authors seek here the asymptotic solution that corresponds to forcing, which is constant over time. The surface boundary conditions at the limits correspond to a west wind of 10 m s^{-1} and to a relaxation condition for the constant buoyancy. These simple conditions allow the main characteristics of geophysical flow be obtained, while at the same time retaining a solution that is smooth enough to be represented on a 'small' number of modes.

The study domain is assumed to be situated at a latitude roughly identical to that of the Mediterranean for which the range of the Coriolis force is in the order of 10^{-4} rad s^{-1}.

2.4.2. Spectrum analysis. Observation of the energy spectrum is the most suitable criterion to ensure that the simulation represents a coherent flow. If this spectrum does not present a sufficient decrease and if the smallest modes play an important role, then simulation results cannot be considered as being satisfactory. The spectral range used to represent flow is thus not large enough and the energy that should be dissipated naturally at a smaller scale is dissipated at the cut-off frequency by an increase in the intensity of these modes [15].

From a practical point of view, it is difficult to increase the width of the spectral range (the NLG was developed to achieve this). Thus, the only way of improving the quality of the simulation is to increase the viscosity of the fluid. The viscosity coefficient used is usually of a greater magnitude than that of turbulent viscosity and allows the modelling (rough approximation) of dissipation beyond the cut off frequency.

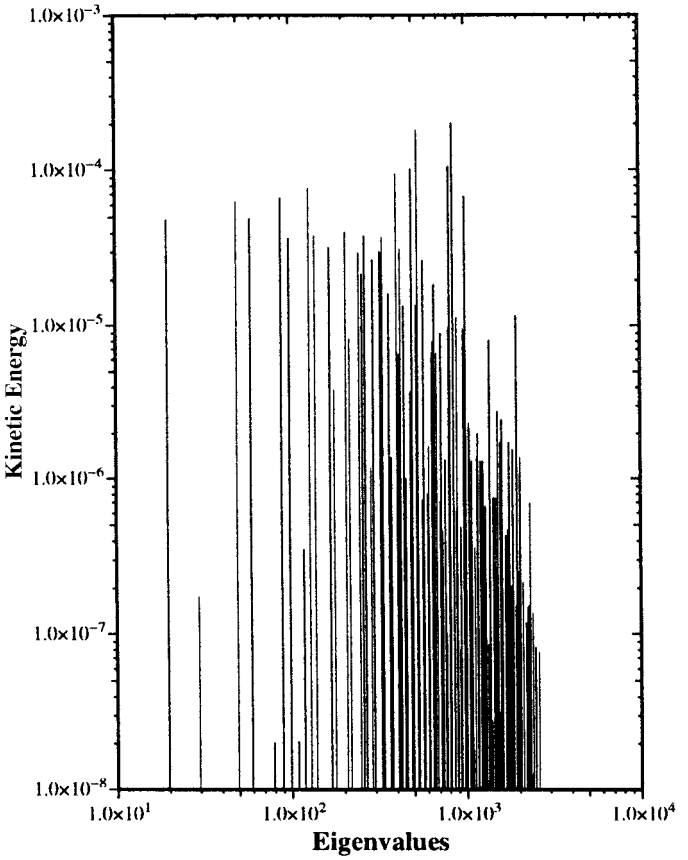

Figure 6. Spectrum of **u**.

For the simulations presented here, the authors have used 1000 three-dimensional modes. Due to the splitting of the basis into two (one part into a gradient and the other into a curl), only those structures possessing a minimum length of one fifth of the domain length can be presented. In the vertical direction, the scale of representative length is in the order of one tenth of the height. This detail seems necessary in order to correctly represent the pronounced gradients in the surface layer.

Details of the same order of magnitude on the scalar fields necessitates the use of approximately 500 modes. Thus, even if the characteristics proper to the vertical component of the basis are used, it is close to 20 million coefficients that must be stocked and as many loops carried out for each evaluation of the scalar advection terms.

In Figure 6, the authors have represented the shape of the kinetic energy spectrum when the asymptotic solution has been reached. This spectrum is consistent with that produced by Charney [13]. The decrease of the spectrum, however, was only obtained by using a horizontal viscosity coefficient of 10^5 and a vertical viscosity coefficient of 10^{-2}. These values are higher than those given in the literature and are linked to the limited spatial discretization. In Figure 7, they have represented the scalar spectrum of the asymptotic solution. In this figure, a rapid decrease can be seen but which is less strong than that observe for the kinetic energy spectrum. The most significant modes are those affected by the relaxation condition at the surface. The other modes are only affected by the advection terms.

2.4.3. Effect of the different terms. The following figures present the relative effects of the different terms that appear in the momentum equation. On this occasion, the authors have chosen to classify the modes in increasing order of appearance in the spectrum while also distinguishing from modes possessing multiple natural values. In Figure 8, they have represented the absolute value of $\int_{\Gamma_s} \tau^s \boldsymbol{\varphi}_i \, d\Gamma_s$ according to the mode i. This term represents the influence of the limit conditions (wind) on the evolution of the mode i, that the entire spectral range is influenced by the wind. All of the modes possessing the same horizontal component are subjected to the same influence by external forces (with the exception of the barotrope component, which possesses one multiplicative coefficient more or less).

In Figure 9, it can be observed that the highest frequencies almost completely dissipate this energy (diffusion is almost equal to excitation), whereas at the lowest frequencies this energy is only partially dissipated, the rest being redistributed to the flow. Diffusion is also observed occurring on a large number of modes that are indirectly excited by the various couplings.

The two following spectra (Figures 10 and 11) represent the influences of the Coriolis force and that of the pressure gradient in the equations respectively. These two terms are dominant in domains of very large dimension (oceans) in which they represent the geostrophic balance. In the present case, it should be noted that they play a fundamental role in the distribution of energy. The influence of the Coriolis force decreases with decreasing frequencies, although this

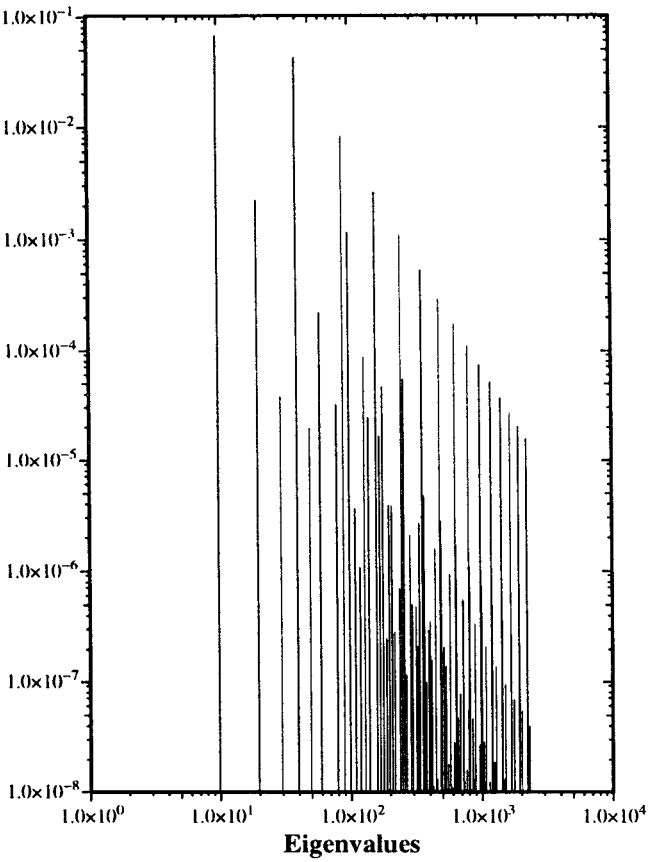

Figure 7. Scalar spectrum.

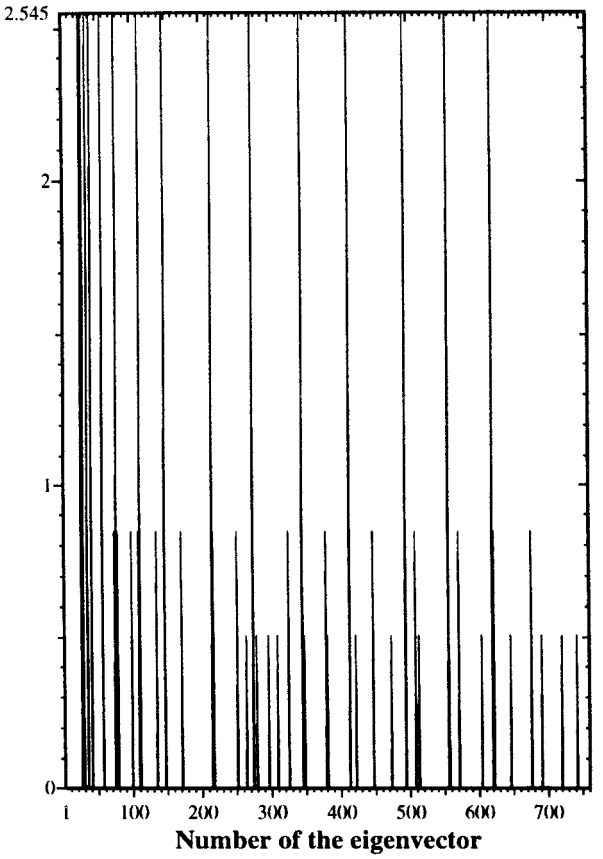

Figure 8. Distribution of τ^s.

influence remains important in the calculation of the smallest structures. The kinetic energy spectrum does indeed indicate that the Coriolis force mainly originates from the lower frequencies of the spectrum, which are those frequencies possessing the most energy. In the simulation carried out, the pressure gradient greatly influences a small number of modes. This is due to the particularly simple shape of the surface relaxation condition dictated by buoyancy. For the case of a simulation of the Mediterranean, the temperature conditions are sufficiently homogeneous at the surface and the results should be largely similar. It is thus reasonable to only consider the main components of the scalar field in the estimation of velocity. Finally, the last spectrum which is observed in this simulation corresponds to the influence of the advection terms in the buoyancy equation (Figure 12). This influence is seen to decrease exponentially. The spectra examined above are identical for both the classical Galerkin and NLG methods.

The elimination of modes greater than n_1 for velocity and m_1 for the scalars allows the same spectrum of influence to be obtained.

2.4.4. Results relative to use of the NLG method. Figure 13 presents the variation of parameter n_1 during the simulation (assessed every ten time steps). These variations correspond to values of parameters $\varepsilon_{\mathbf{u}}$ and ε_b of $5 \cdot 10^{-0.2}$ that appear to be the most suitable for the simulations carried out, the period during which the variation of the small scales are 'frozen'

is fixed at ten time steps. The total kinetic energy contained in the 'quasi-static' modes is always less than 5% of total kinetic energy. This represents an important saving of time in the speed of calculation as, for each iteration, only 100 or 200 modes are estimated as opposed to the 1000 modes initially provided for. It would appear that the parameter n_1 increases slightly during the simulation. It is mainly the evolution of the large structures, which start off at a velocity at rest, that will generate smaller structures and lead to the increasing complexity of flow (the very high diffusion phenomena, however, lead to the development of turbulence).

In Tables I and II, the authors have included the variations in the magnitude of $Ec(\mathbf{u})$ and $Ep(b)$ at different moments in time for both the classical Galerkin and NLG methods. The kinetic energy reaches its maximum level after the first 10 h, and subsequently decreases slightly while E_b increases. A portion of the kinetic energy is transformed into potential energy by destabilization of the stratification. The variation between the two calculation methods remains very small and tends to become zero for the asymptotic solution. The asymptotic convergence is obtained after 10^5 time increments of 10^2 s, which corresponds to 115 days in real time (the CPU time is in the order of 28 h for the usual Galerkin method and 7 h for the NLG method). The savings of approximately 75% on the number of operations is mainly realized during the assessment of the non-linear advection terms.

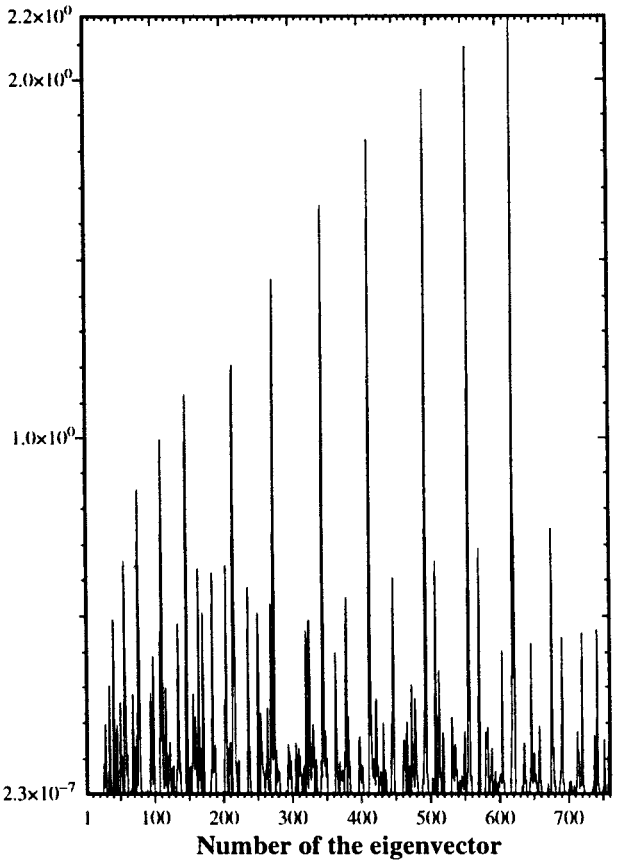

Figure 9. Influence of diffusion.

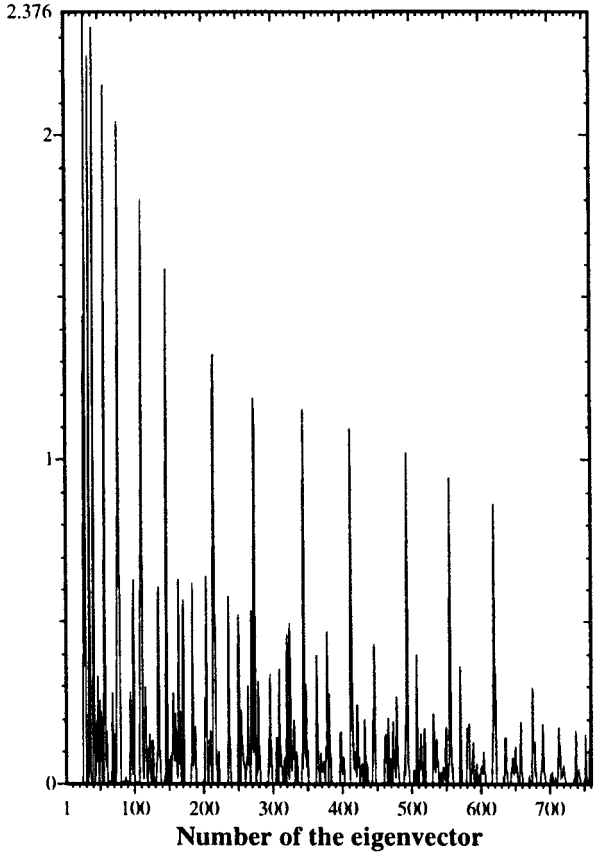

Figure 10. Influence of Coriolis.

2.4.5. Representation of the three-dimensional fields. In Figures 14 and 15, the authors present a three-dimensional view of the velocity field at the edges of the domain as well as a vertical section along the east–west axis. Classical results can be observed, such as the velocity forming a 45° angle at the surface with respect to wind direction. This observation is in agreement with the Ekman theory (Figure 16).

In the same way, a reversal of velocity according to the vertical can be observed in the vertical section (Figure 15) that also corresponds to the Ekman spiral (Figure 16) and to a deformation of stratification leading to the development of a pronounced thermocline (Figure 17) in the southeastern part of the domain (the surface layer is well-mixed).

3. STUDY OF A GENERAL CASE: USE OF THE σ TRANSFORMATION

In this section, the authors present the more general case of a domain having a variable bathymetry. In order to use the same special basis as was used for the case of a flat bottom, a geometric transformation must be applied to the study domain so as to give it a 'cylindrical' shape (constant height).

3.1. The equations transformed by σ

The authors apply the following transformation

$$\begin{Bmatrix} x \\ y \\ z \end{Bmatrix} \underset{\sigma}{\rightarrow} \begin{cases} x_1 = x \\ x_2 = y \\ x_3 = \dfrac{z+h}{h} \end{cases} \quad \text{with } h(x_1, x_2, t) = H(x_1, x_2) + \zeta(x_1, x_2, t).$$

For example, the horizontal gradient of a function belonging to the transformed domain is given by

$$\nabla A = \begin{pmatrix} \dfrac{\partial A}{\partial x_1} \\ \dfrac{\partial A}{\partial x_2} \end{pmatrix},$$

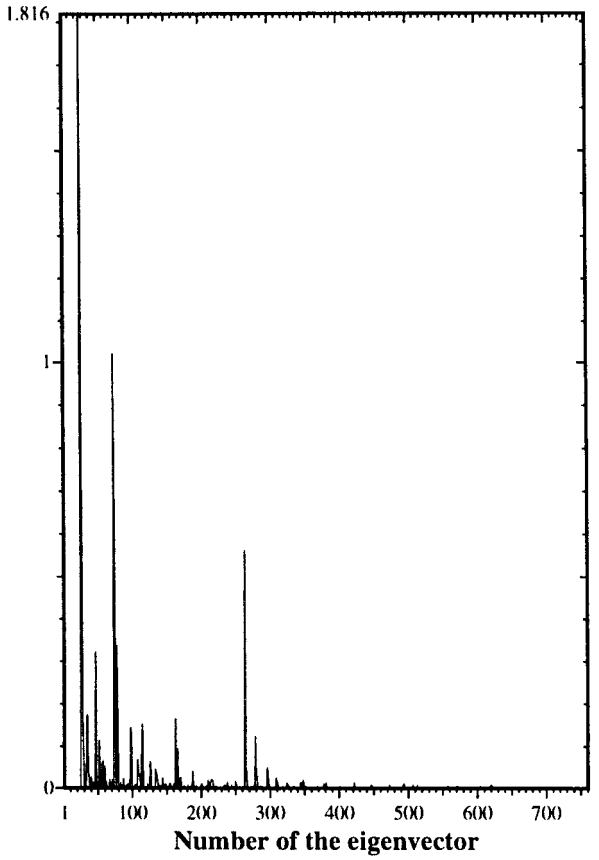

Figure 11. Influence of the pressure gradient.

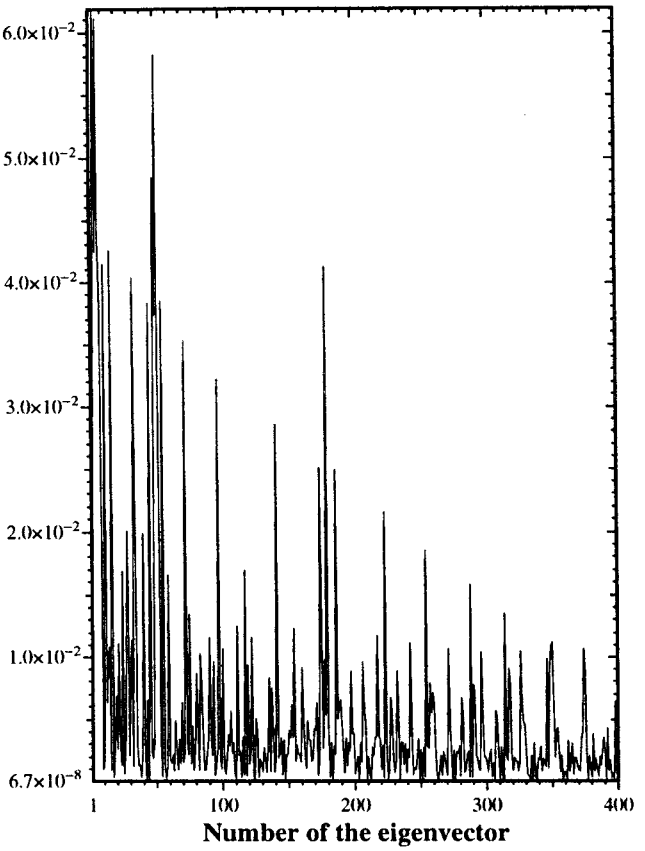

Figure 12. Scalar advection.

with the relationship

$$\begin{pmatrix} \dfrac{\partial A(x,y,z)}{\partial x} \\ \dfrac{\partial A(x,y,z)}{\partial y} \end{pmatrix} = \begin{pmatrix} \dfrac{\partial A(x_1,x_2,x_3)}{\partial x_1} \\ \dfrac{\partial A(x_1,x_2,x_3)}{\partial x_2} \end{pmatrix} + \left[\frac{1-x_3}{h} \begin{pmatrix} \dfrac{\partial H}{\partial x_1} \\ \dfrac{\partial H}{\partial x_2} \end{pmatrix} - \frac{x_3}{h} H \begin{pmatrix} \dfrac{\partial \zeta}{\partial x_1} \\ \dfrac{\partial \zeta}{\partial x_2} \end{pmatrix} \right]. \tag{3.1}$$

The equations in the domain transformed by σ are thus as follows

$$\frac{\partial \mathbf{u}}{\partial t} + B(\mathbf{u},\mathbf{u}) + \omega\alpha(\mathbf{u}) = \frac{1}{h^2}\frac{\partial}{\partial x_3}\left(\nu \frac{\partial \mathbf{u}}{\partial x_3}\right) - F(b) + \mu D(\mathbf{u}), \tag{3.2}$$

$$\frac{\partial b}{\partial t} + C(\mathbf{u}, b) = \frac{1}{h^2}\frac{\partial}{\partial x_3}\left(\nu_b \frac{\partial b}{\partial x_3}\right) + \mu_b D_b(b), \tag{3.3}$$

$$\frac{\partial \zeta}{\partial t} + \nabla(h\bar{\mathbf{u}}) = 0, \tag{3.4}$$

$$\bar{\mathbf{u}} = \int_0^1 \mathbf{u}\, \mathrm{d}x_3; \qquad \mathbf{u} = \bar{\mathbf{u}} + \mathbf{u}'; \qquad v_3 = \int_{x_3}^1 \frac{\nabla(h\mathbf{u}')}{h}\, \mathrm{d}\xi, \tag{3.5}$$

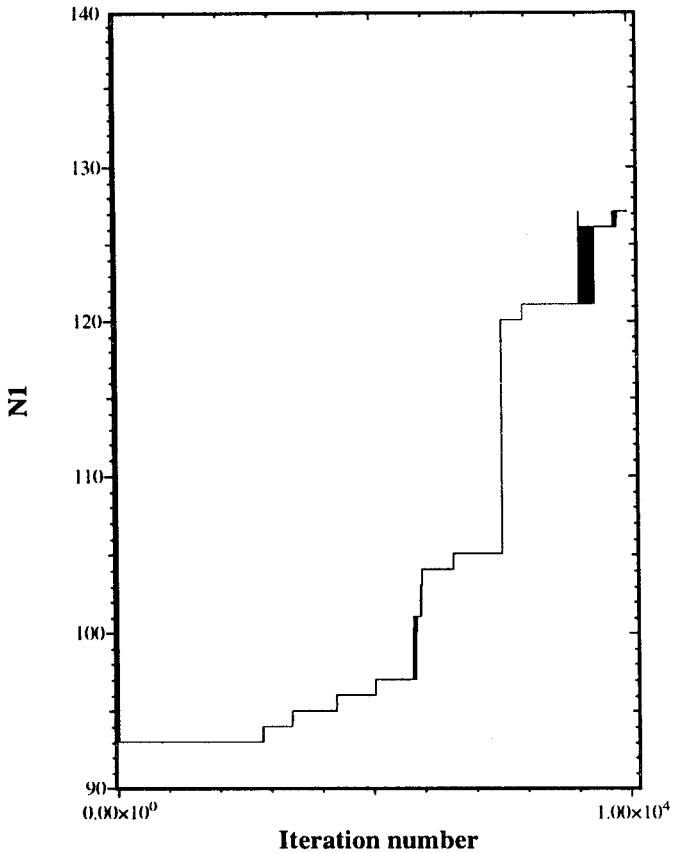

Figure 13. Evolution of parameter n_1.

$$F(b) = -\nabla\left[h\int_{x_3}^{1} b(\xi)\,\mathrm{d}\xi\right] + [(1-x_3)\nabla H - x_3\nabla\zeta]b + \nabla\left(\frac{Pa}{\rho_0} + g\zeta\right), \tag{3.6}$$

where the functions D and D_b represent horizontal dissipation.

3.2. Solving using the Galerkin method

3.2.1. Weak formulation. The authors are unable to demonstrate the existence of a solution to the problem examined. They will nevertheless seek an approximation to its solution (assuming that such a solution exists).

Table I. Comparison of the kinetic energy

t	$Ec(\mathbf{u})$ (SI unit)		
(days)	GU ($\times 10^{13}$)	GNL ($\times 10^{13}$)	Difference ($\times 10^{13}$)
0.5	0.27681722	0.27855531	−0.00173809
1	0.26475030	0.26618917	−0.00143887
3	0.26352396	0.26423784	−0.00071388
12	0.25987721	0.26137682	−0.00149961
58	0.24095331	0.24173594	−0.0078263
115	0.22121153	0.22123632	−0.0002479

Table II. Comparison of the buoyancy norm

t	$Eb(b)$ (SI units)		
(days)	GU ($\times 10^{17}$)	GNL ($\times 10^{17}$)	Difference ($\times 10^{17}$)
0.5	0.29365523	0.29632897	0.00267374
1	0.30785368	0.30735294	0.00050074
3	0.32141455	0.31875101	0.00266354
12	0.36078654	0.35993683	0.00084971
58	0.41673693	0.41635970	0.00037723
115	0.42117398	0.42100591	0.00016807

Given $(\mathbf{u}_0, b_0, h_0)$, the authors then seek $(\mathbf{u}, b, h)$, the solution of

$$\left(\frac{\partial \mathbf{u}}{\partial t}, \boldsymbol{\varphi}_k\right) - \frac{1}{2}(\mathbf{u}^2, \operatorname{div} \boldsymbol{\varphi}_k) + (\operatorname{curl} \mathbf{u}\alpha(\mathbf{u}), \boldsymbol{\varphi}_k) + \left(v_3 \frac{\partial \mathbf{u}}{\partial x_3}, \boldsymbol{\varphi}_k\right) + (\omega\alpha(\mathbf{u}), \boldsymbol{\varphi}_k)$$
$$= -(F(b), \boldsymbol{\varphi}_k) + \int_{\Omega_x} \left[\frac{\tau^s}{h} \boldsymbol{\varphi}_k(x, y, 1) - \frac{\tau^b}{h} \boldsymbol{\varphi}_k(x, y, 0)\right] d\Omega_x - \left(\frac{\tilde{\nu}}{h^2} \frac{\partial \mathbf{u}}{\partial x_3}, \frac{\partial \boldsymbol{\varphi}_k}{\partial x_3}\right) + (\mu D(\mathbf{u}), \boldsymbol{\varphi}_k)$$
$$\forall \boldsymbol{\varphi}_k \in \mathscr{V}, \tag{3.7}$$

where $\boldsymbol{\varphi}_k$ are elements of the basis defined in Section 1.2.1.

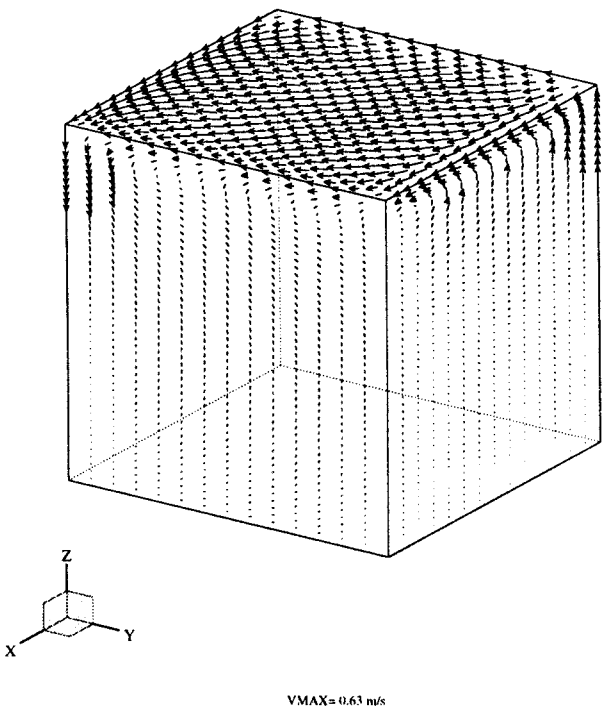

Figure 14. 3D view of the velocity field.

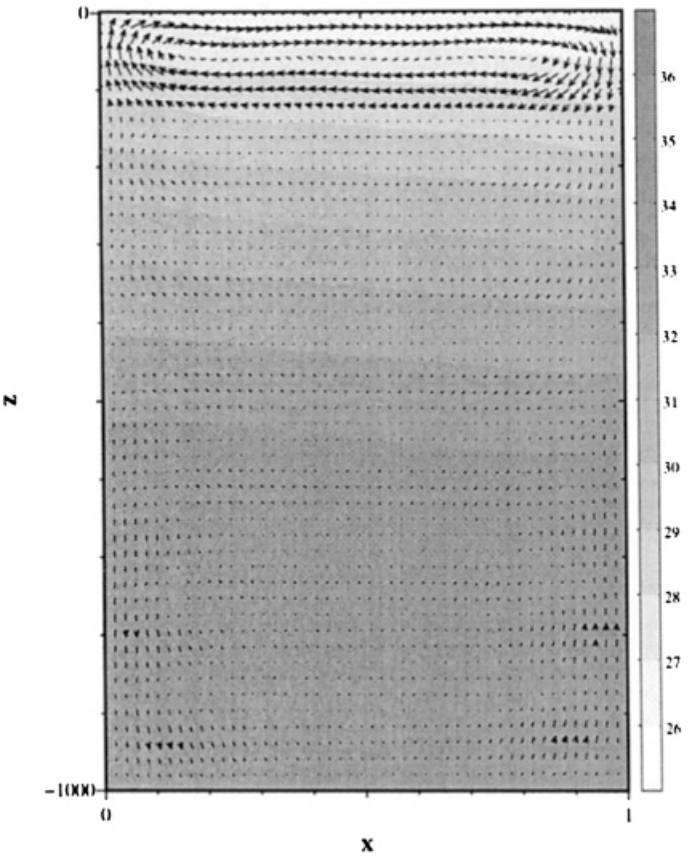

Figure 15. Vertical section in the middle of the domain ($y = 500$ km).

$$\left(\frac{\partial b}{\partial t}, \phi_k\right) + (\mathbf{u}\nabla b, \phi_k) + \left(v_3 \frac{\partial b}{\partial x_3}, \phi_k\right)$$
$$= \int_{\Omega_x} \frac{F^b}{h} \phi_k(x, y, 0)\, \mathrm{d}\Omega_x - \left(\frac{\tilde{v}_b}{h^2} \frac{\partial b}{\partial x_3}, \frac{\partial \phi_k}{\partial x_3}\right) + (\mu_b D_b(b), \phi_k) \quad \forall \phi_k \in H^1(\Omega), \tag{3.8}$$

where the ϕ_k are the functions defined in Section 1.2.4.

$$\left(\frac{\partial \zeta}{\partial t}, p_k\right) - (\bar{\mathbf{u}}h, \nabla p_k) = 0 \quad \forall p_k \in H^1(\Omega_x), \tag{3.9}$$

where p_k are functions that are the solutions of problem (Pg) with

$$(F(b), \boldsymbol{\varphi}) = \left(H \int_{x_3}^{1} b(\xi)\, \mathrm{d}\xi, \operatorname{div} \boldsymbol{\varphi}\right) - ((1 - x_3)H\nabla b, \boldsymbol{\varphi}) - ((1 - x_3)Hb, \operatorname{div} \boldsymbol{\varphi})$$
$$+ (x_3 \zeta \nabla b, \boldsymbol{\varphi}) + (x_3 \zeta b, \operatorname{div} \boldsymbol{\varphi}),$$
$$(D(\mathbf{u}), \boldsymbol{\varphi}) = -(\nabla \cdot \mathbf{u}, \nabla \cdot \boldsymbol{\varphi}) - (\operatorname{curl} \mathbf{u}, \operatorname{curl} \boldsymbol{\varphi}) - \left(\left(\frac{1 - x_3}{h} \nabla h\right) \frac{\partial \mathbf{u}}{\partial x_3}, \nabla \cdot \boldsymbol{\varphi}\right)$$
$$+ \left(\left[\nabla \cdot \mathbf{u} + \left(\frac{1 - x_3}{h} \nabla h\right) \frac{\partial \mathbf{u}}{\partial x_3}\right] \frac{\nabla h}{h}, \boldsymbol{\varphi}\right) - \left(\left[\nabla \cdot \mathbf{u} + \left(\frac{1 - x_3}{h} \nabla h\right) \frac{\partial \mathbf{u}}{\partial x_3}\right] \left(\frac{1 - x_3}{h} \nabla h\right), \frac{\partial \boldsymbol{\varphi}}{\partial x_3}\right)$$

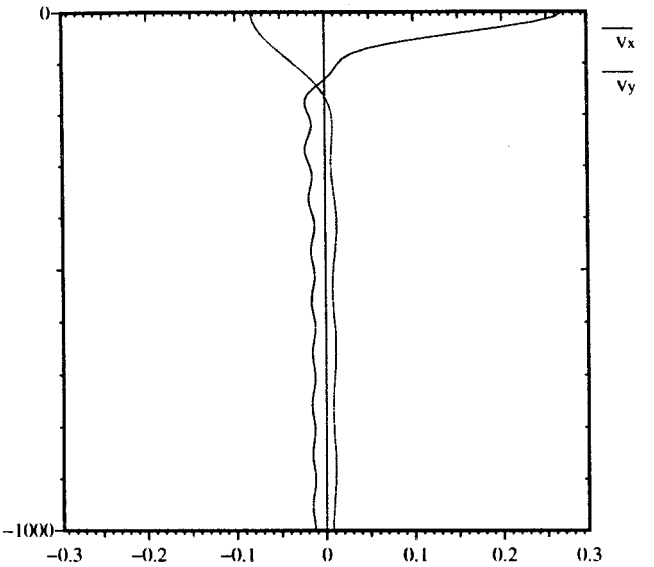

Figure 16. Ekman spiral at the centre of the domain.

$$+\left(\left(\frac{1-x_3}{h}\,\mathrm{Curl}\,h\right)\frac{\partial \mathbf{u}}{\partial x_3},\mathrm{curl}\,\boldsymbol{\varphi}\right)-\left(\left[\mathrm{curl}\,\mathbf{u}-\left(\frac{1-x_3}{h}\,\mathrm{Curl}\,h\right)\frac{\partial \mathbf{u}}{\partial x_3}\right]\frac{\mathrm{Curl}\,h}{h},\boldsymbol{\varphi}\right)$$
$$+\left(\left[\mathrm{curl}\,\mathbf{u}-\left(\frac{1-x_3}{h}\,\mathrm{Curl}\,h\right)\frac{\partial \mathbf{u}}{\partial x_3}\right]\left(\frac{1-x_3}{h}\,\mathrm{Curl}\,h\right),\frac{\partial \boldsymbol{\varphi}}{\partial x_3}\right)$$

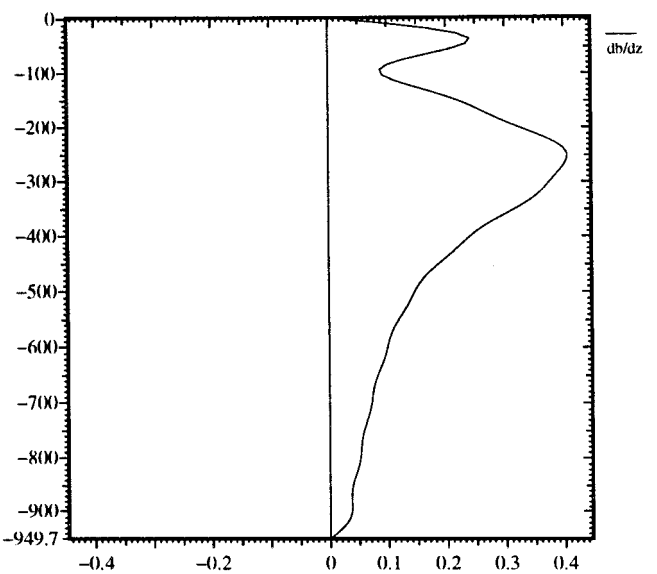

Figure 17. Brunt–Vaïsälä frequency in the southeastern section.

$$+\int_{\Omega_x}\left[\frac{1-x_3}{h}\nabla h\left(\nabla\cdot\mathbf{u}+\left(\frac{1-x_3}{h}\nabla h\right)\frac{\partial\mathbf{u}}{\partial x_3}\right)\boldsymbol{\varphi}\right]_0^1 \mathrm{d}\Omega_x$$
$$+\int_{\Omega_x}\left[\frac{1-x_3}{h}\,\mathrm{Curl}\,h\left(\mathrm{curl}\,\mathbf{u}-\left(\frac{1-x_3}{h}\,\mathrm{Curl}\,h\right)\frac{\partial\mathbf{u}}{\partial x_3}\right)\boldsymbol{\varphi}\right]_0^1 \mathrm{d}\Omega_x$$

and

$$(D_b(b),\phi)=-(\nabla b,\nabla\phi)-\left(\left(\frac{1-x_3}{h}\nabla h\right)\frac{\partial b}{\partial x_3},\nabla\phi\right)+\left(\left[\nabla b+\left(\frac{1-x_3}{h}\nabla h\right)\frac{\partial b}{\partial x_3}\right]\frac{\nabla h}{h},\phi\right)$$
$$-\left(\frac{1-x_3}{h}\nabla h\left[\nabla b+\left(\frac{1-x_3}{h}\nabla h\right)\frac{\partial b}{\partial x_3}\right],\frac{\partial\phi}{\partial x_3}\right)$$
$$+\int_{\Omega_x}\left[\frac{1-x_3}{h}\nabla h\left(\nabla b+\left(\frac{1-x_3}{h}\nabla h\right)\frac{\partial b}{\partial x_3}\right)\phi\right]_0^1 \mathrm{d}\Omega_x.$$

3.2.2. An approximate solution. The authors seek $(\mathbf{u}_n(\mathbf{x},t), b_n(\mathbf{x},\mathrm{it})h_m(\mathbf{x},t))$, the approximate solution of the previous equations. They have the following decompositions

$$\mathbf{u}_n(\mathbf{x},t)=\sum_{i=1}^{n}\mathscr{X}_i(t)\boldsymbol{\varphi}_i(\mathbf{x}), \tag{3.10}$$

$$b_m(\mathbf{x},t)=\sum_{i=1}^{m}\mathscr{Y}_i(t)\phi_i(\mathbf{x}), \tag{3.11}$$

$$h_r(x_1,x_2,t)=\sum_{i=1}^{r}\mathscr{Z}_i(t)p_i(x_i,x_2). \tag{3.12}$$

It is preferable to differentiate the barotrope component $\bar{\mathscr{X}}$ from the velocity and its barocline component $\mathscr{X}'$. The characteristic time associated with the surface waves are indeed much lower than the characteristic times seen for the other phenomena that the authors wish to examine.

The solution to the equation system can be approached by solving the first-order differential equation system possessing the following constant coefficients

$$\dot{\bar{\mathscr{X}}}_i=\sum_{j=1}^{n}\mathscr{X}_jXX(i,j)+\sum_{j=1}^{m}\mathscr{Y}_jXY(i,j)+\sum_{k=1}^{r}\mathscr{Z}_jXZ(i,j)+\sum_{j=1}^{n}\sum_{k=1}^{n}\mathscr{X}_j\mathscr{X}_kXXX(i,j,k), \tag{3.13}$$

$$\dot{\mathscr{X}}'_i=\sum_{j=1}^{n}\mathscr{X}_jXX(i,j)+\sum_{j=1}^{m}\mathscr{Y}_jXY(i,j)+\sum_{j=1}^{m}\sum_{k=1}^{r}\mathscr{Z}_kXYZ(i,j,k)$$
$$+\sum_{j=1}^{n}\sum_{k=1}^{n}\mathscr{X}_j\mathscr{X}_kXXX(i,j,k), \tag{3.14}$$

$$\dot{\mathscr{Y}}_i=\sum_{j=1}^{m}\mathscr{Y}_jYY(i,j)+\sum_{j=1}^{n}\sum_{k=1}^{n}\mathscr{X}_j\mathscr{Y}_kYXY(i,j,k), \tag{3.15}$$

$$\dot{\mathscr{Z}}_i=\sum_{j=1}^{n}\sum_{k=1}^{n}\vec{\mathscr{X}}_j\mathscr{Z}_kZXZ(i,j,k). \tag{3.16}$$

The terms XX, XY, XZ, XXX, YY, YXY, XYZ and ZXZ are constant and on the study domain, represent integrals of basis function combinations.

3.3. The non-linear Galerkin method

3.3.1. The cut-off frequency. The numerical tests reveal that the kinetic energy associated with the horizontal component of velocity is substantially higher than that of the vertical component. A good approximation of the total kinetic energy is given by $Ec(\mathbf{u}_n)$. The choice of the cut-off frequency associated with velocity is smaller than the value of n_1, which satisfies:

$$\frac{Ec(\hat{\mathbf{u}}_{n_1})}{Ec(\mathbf{u}_{n_1})} < \varepsilon_{\mathbf{u}}. \tag{3.17}$$

During the uncoupling of the barotrope part described below, a cut-off frequency for the barotrope component must be defined. This frequency is determined in much the same way as for the shallow water equations by the value of $\bar{n}_1$, which satisfies the relationship

$$\frac{Ec(\hat{\bar{\mathbf{u}}}_{\bar{n}_1})}{Ec(\bar{\mathbf{u}}_{\bar{n}_1})} < \varepsilon_{\mathbf{u}}. \tag{3.18}$$

The cut-off frequency associated with the elevation (written r_1) is linked to $\bar{n}_1$ by a relationship proper to the numeric method. In the absence of dissipation in the elevation evolution equation, the numerical resolution necessitates the use of an equal number of grad p_i functions for barotropic velocity as of p_i functions for elevation.

3.3.2. Barotrope–barocline uncoupling. The presence of the hyperbolic equation that describes the variations at the surface leads to taking into consideration the external gravity waves that exhibit extremely high phases (tens of $\mathrm{m\,s^{-1}}$). The resolution of these waves requires a small time increment in order to verify the CFL criterion, which represents a substantial drawback to the numerical method.

The authors limit the costs linked to this constraint by implementing an uncoupling of the resolution time increments between the barotropic and baroclinic components. They will solve a system that includes the barotropic velocity and elevation equations by using a small time step. To solve the more complete system, they will then use a larger time step.

The barotropic velocity is broken down in the following way:

$$\bar{\mathbf{u}}_n(\mathbf{x}, t) = \sum_{i=1}^{n_1} \bar{X}_i(t)\boldsymbol{\varphi}_i(\mathbf{x}) + \sum_{i=n_1+1}^{n} \bar{X}_i(t)\boldsymbol{\varphi}_i(\mathbf{x}). \tag{3.19}$$

The first sum ($\bar{\mathbf{u}}_{n_1}$) represents the large barotropic structures, while the second ($\hat{\bar{\mathbf{u}}}_{n_1}$) represents the small barotropic structures.

The authors apply a decomposition of the same sort to the elevation h.

$$h_r(\mathbf{x}, t) = \sum_{i=1}^{r_1} Z_i p_i + \sum_{i=r_1+1}^{r} Z_i p_i. \tag{3.20}$$

The first sum (written h_{r_1} hereafter) represents the large elevation structures, while the second (which will be termed $\hat{h}_{r_1}$) represents the small structures.

The authors write $\mathbf{P}h_{r_1}$, which is the projection onto the r_1 first p_i functions and $\mathbf{Q}h_{r_1}$, the projection onto the $(r - r_1)$ following p_i functions.

If DH is written as being the sum of the terms present in the momentum equation projected onto the largest elevation components and $D\hat{H}$ as the same sum projected onto the smallest structures, then the following approximation can be used:

$$DH = \int_t^{t+\Delta t} \mathbf{P}\mathrm{h}_{m_1}(\mathrm{div}(\bar{\mathbf{u}}_{n_1}(\theta)h_{m_1}(\theta))) + \mathbf{P}\mathrm{h}_{m_1}(\mathrm{div}(\bar{\mathbf{u}}_{n_1}(\theta)\hat{h}_{m_1}(t)))\,\mathrm{d}\theta. \tag{3.21}$$

The numerical tests reveal that a good behaviour estimate for the small elevation components is given by

$$\widehat{DH} = \Delta t \mathbf{Q} \mathrm{h}_{n_1}(\mathrm{div}(\tilde{\mathbf{u}}_{n_1}(t+\Delta t) h_{r_1}(t+\Delta t))). \tag{3.22}$$

During the solving of the barotropic elevation system, the effect of the barocline component is assumed to be constant and corresponds to the component calculated for the previous barocline time increment.

3.3.3. Application of the NLG method to the diffusion operator. In Section 2.2.8, the authors presented the application of the NLG method for the treatment of horizontal diffusion. The properties of the operator allows the squaring method to be applied, which allows an accurate integration.

During the transformation σ, however, the projection operator L^2 no longer permutes with the horizontal diffusion operator. The horizontal diffusion thus becomes a source of energy exchange in much the same way as the variable vertical diffusion. The authors propose the following estimates, which yield satisfactory numerical results.

$$\mathrm{DIFF} = \int_t^{t+\Delta t} \mathbf{P}_{n_1}(D(\mathbf{u}_{n_1}(\theta)))\,\mathrm{d}\theta + \Delta t \mathbf{P}_{n_1}(D(\hat{\mathbf{u}}_{n_1}(t))), \tag{3.23}$$

$$\widehat{\mathrm{DIFF}} = \int_t^{t+\Delta t} \mathbf{Q}_{n_1}\left(D\left(\hat{\mathbf{u}}_{n_1}(\theta)\right)\right)\mathrm{d}\theta + \Delta \mathrm{t} \mathbf{Q}_{n_1}(D(\mathbf{u}_{n_1}(t+\Delta t))). \tag{3.24}$$

An identical expression is used for the diffusion operator associated with buoyancy.

4. CONCLUSIONS

In this study, The authors have applied the non-linear Galerkin method to geophysical fluids in order to increase the level of spatial discretization. In this first step, They compared the results generated by the CG and NLG methods in order to validate this approach and to understand the fundamental mechanisms of mode coupling. In so doing, they have revealed the presence of simplified laws of interaction in the estimation of the smaller flow components. These are then expressed as being only a function of the largest components.

This approach allows a direct estimate to be made of these small structures, the effect of which in total flow can be approximated to be quasi-static during 'short' periods of time. The savings in time are partly due to the decrease in the mean number of calculations at each iteration but also to the elimination of the numerical instabilities during the estimates of coupling between small structures, which allows the implementation of a larger time increment. In addition to being efficient in the estimation of non-linear terms, this method is also interesting for the estimation of some linear terms. Indeed, even in the absence of non-linear terms in the momentum equation, the Coriolis force and the pressure forces are responsible for the distribution of energy over a large spectral band, which justifies the use of NLG method.

The NLG method can be considered to be a modelling of the exchanges occurring at an intermediate scale between the large structures, explicitly solved by the equations, and the small structures roughly modelled by the diffusion terms. This method does not correspond to a modelling of turbulence but rather to a modelling of phenomenon of intermediate mesh. Although the simulations presented in this document are performed by using simple geometric shapes, it seems obvious that the use of a more complicated boundary will generate a greater number of small sized vortexes. The NLG method, therefore, appears to represent an

interesting approach in the near future as the calculation capacity remains well below the needs of these types of simulations.

In the next step, the authors will show the numerical results in the case of the σ transform and the use of the non-homogeneous boundary conditions of open sea (see also [21]).

REFERENCES

1. P. Orenga, 'Construction d'une base spéciale pour la résolution de quelques problèmes d'océanographie physique en dimension deux', *CRAS*, **314**, 587–590 (1992).
2. P. Orenga, 'Un théorème d'existence de solutions d'un problème de shallow water', *Arch. Rational Mach. Anal.*, **130**, 183–204 (1995).
3. A. Debussche, T. Dubois and R. Temam, 'The non-linear Galerkin method: A multi-scale method applied to the simulation of homogeneous turbulent flow', *Theorical and Computational Fluid Dynamic*, 1995, preprint.
4. T. Dubois, 'Simulation numérique d'écoulements homogènes et non homogènes par des méthodes multi-résolution', *Thèse de Doctorat*, Université de Paris-Sud, Centre d'Orsay, 1993.
5. F. Jauberteau, 'Résolution numérique des équations de Navier–Stokes instationnaires par méthodes spectrales—Méthode de Galerkin non-linéaire', *Thèse de Doctorat*, Université de Paris-Sud, Centre d'Orsay, 1990.
6. B. di Martino and P. Orenga, 'Résolution des équations de shallow water par la méthode de Galerkin non linéaire', *RAIRO*, 1998, in press.
7. J.C.J. Nihoul, *Modèles mathématiques et Dynamique de l'environnement*, Elsevier, Amsterdam, 1977.
8. P. Orenga, F.J. Chatelon and C. Fluixa, 'Analysis of some oceanography physics problems by the Galerkin's method', in *The Mathematics of Models for Climatology and Environment*, NATO Advanced Study, 1995.
9. J.L. Lions, R. Temam and S. Wang, 'On the equation of the large scale ocean', *Non-linearity*, **5**, 1007–1053 (1992).
10. J.C.J. Nihoul, *Modelling of Marine Systems*, Elsevier oceanography series, Elsevier, Amsterdam, 1975.
11. P. Orenga, 'Analyse de quelques problèmes d'océanographie physique', *Thèse d'habilitation*, Université de Corse, Corte, 1992.
12. C. Fluixa, 'Analyse d'un problème d'océanographie physique en dimension trots par la méthode de Galerkin', *These de Doctorat*, Université de Corse, Corte, 1997.
13. J.G. Charney, 'Geostrophic turbulence', *J. Atmos. Sci.*, **28**, 1087–1095 (1971).
14. P.K. Kundu, *Fluid Mechanics*, Academic Press, New York, 1990.
15. M. Lesieur, *Turbulence in Fluids. Fluid Mechanics and its Applications*, 2nd edn., Kluwer Academic, Dordrecht, 1990.
16. C. Foias, O. Manley and R. Temam, 'Sur l'interaction des petits et grands tourbillons dans les écoulements turbulents', *CRAS*, **305**, 497–500 (1987).
17. C. Foias, O. Manley and R. Temam, 'Modelling of the interaction of small and large eddies in two dimensional turbulent flows', M^2AN, **22**, 93–114 (1988).
18. G. Fumes, 'A three-dimensional numerical sea model with eddy viscosity varying piecewise linearly in the vertical', *Cont. Shelf Res.*, **2**, 231–241 (1983).
19. A. Davies, 'On using turbulence energy models to develop spectral viscosity models', *Cont. Shelf Res.*, **11**, 1313–1353 (1991).
20. J.C.J. Nihoul, E. Deleersnijder and S. Djenidi, 'Modelling the general circulation of shelf seas bye 3D k–ε models', *Earth Sci. Rev.*, **26**, 163–189 (1989).
21. F.J. Chatelon and P. Orenga, 'On a non-homogeneous shallow water problem', M^2AN, **31**, 27–55 (1997).

